Global NEST Journal, Vol 27, No 3, 06883

An investigation into the composition of the mineral phase of fly ash using advanced techniques

Longjiao Lv.[1], Liu J.[1], Li F.[2], Mu X.[2], Ren Y.[2], Ren B.[3], Yin F.[1] and Zhu G.[1*]
[1]College of Civil Engineering, Hunan University of Science and Technology, Xiangtan, 411201, Hunan, China
[2]Water source team of Guizhou Coal Geological Bureau, Guiyang 550081, Guizhou, China
[3]School of Earth Sciences and Spatial Information Engineering, Hunan University of Science and Technology, Xiangtan, 411201, Hunan, China
Received: 13/10/2024, Accepted: 27/12/2024, Available online: 02/01/2025
*to whom all correspondence should be addressed: e-mail: zhuguoc@hnust.edu.cn
https://doi.org/10.30955/gnj.06883

Graphical abstract

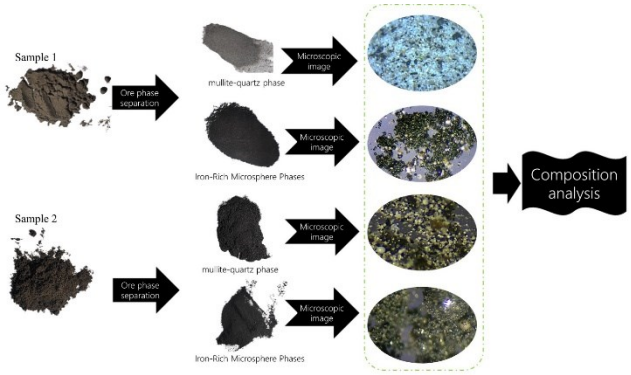

Abstract

Fly ash, a pivotal byproduct of coal combustion in thermal power plants, has yet to be fully harnessed as an abundant resource for metallic elements resources. A comprehensive understanding of its composition is essential for the exploitation of potentially valuable metals. We research the structural makeup of fly ash utilizing cutting-edge technological approaches, with the aim to provide direction for the development and utilization of its metallic element contents. Micro-Raman spectroscopy, in conjunction with analytical techniques such as X-ray fluorescence spectroscopy, X-ray diffraction, and Fourier-transform infrared spectroscopy, were employed to assess the mineralogical composition of fly ash. The results show that the fly ash analyzed in this study was primarily comprised of mineral phases rich in SiO_2, Al_2O_3, and Fe_2O_3. The primary crystalline phases identified were mullite and quartz. Notably, iron-rich microspheres within the fly ash encompass hematite, magnetite and glassy phases. The mullite-quartz phase also identified the presence of organic carbon. In addition to new knowledge of the mineralogical composition of fly ash it also demonstrates the potential of micro-Raman spectroscopy in characterization of the mineralogical composition of this material.

Keywords: Fly ash; mineral phase; micro-raman spectroscopy; thermal power plant

1. Introduction

With the escalating global energy demand, coal remains a pivotal fossil fuel, underpinning power generation and industrial processes. The byproduct of coal combustion, fly ash, is a potential environmental pollution hazard and the potential as a primary resource is ignored (Kumble *et al*. 2024). Fly ash is primarily composed of elements like silicon, aluminum, iron, and calcium, and the morphology and distribution of these elements is critical to exploit any potential as a resource (Abbas *et al*. 2024, Gadore *et al*. 2024) . However, fly ash exhibits a diverse chemical composition, a complex mineral assemblage, and significantly varying physical properties (Saha *et al*. 2025) . In fact, various studies have identified approximately 316 minerals belonging to 188 mineral groups in different fly ash samples (Vassilev *et al*. 2005) . Consequently, conducting a thorough analysis of its mineralogical composition and exploring avenues for its further utilization is imperative to advance sustainable resource management and environmental conservation.

Currently, a range of analytical methodologies, including X-ray fluorescence spectroscopy (XRF), X-ray diffraction (XRD), Fourier-transform infrared spectroscopy (FT-IR), scanning electron microscopy (SEM), and associated physical separation and chemical leaching techniques, are employed to assess the structural attributes of fly ash. For instance, Bao(Bao 2023) utilized SEM-EDX and XRD to examine the composition of magnetic beads of varying sizes in fly ash. Andrew *et al*.(Witte *et al*. 2024) combined SEM-EDS and Raman spectroscopy to scrutinize particle morphology, crystallinity, and the degree of polymerization of the glass phase in fly ash. Chijioke *et al*. (Egole *et al*. 2024) characterized two clay deposits in southeastern Nigeria, blended with feldspar and quartz, through chemical analysis, XRF, powder XRD, SEM, and thermal analysis. Niyogi *et al*. (Niyogi *et al*. 2018) analyzed the chemical makeup of silicate glass spheres in fly ash

using FT-IR and Raman spectroscopy. Tiwari *et al*.(Tiwari *et al*. 2014) investigated the properties of raw coal, fly ash, and bottom ash sourced from multiple power plants in India, leveraging XRF and XRD to assess elemental concentrations and calculate enrichment rates. While these characterization methods can indeed reveal the characteristics of fly ash and its mineral compositions, they are not without limitations(Bandopadhyay 2010) . For example, XRD and XRF struggle to gather localized data or conduct analyses at the single-particle level, and they have difficulties in accurately analyzing amorphous phases(Vassilev *et al*. 2005) . However, Raman micro-spectroscopy offers a potential solution to these shortcomings. Krishna *et al*.(Polavaram and Garg 2021) successfully employed Raman spectroscopy to quantitatively identify eight secondary phases in cement clinkers with high confidence, including anhydrite, tanzanite, and potassium sulfate. Similarly, Kirkpatrick *et al*.(Kirkpatrick *et al*. 1997) used Raman spectroscopy to perform in-depth analyses of complex mineral compositions, identifying significant Raman spectral signals in the wider ranges of 1080 cm^{-1}, 950-1010 cm^{-1}, and 870-900 cm^{-1}, which are strong indicators of the presence of symmetric stretching vibrations of Q^3, Q^2, and Q^1 silicate tetrahedra, respectively. Currently, there is a paucity of research utilizing micro-Raman spectroscopy to analyze the mineral phase composition of fly ash, highlighting the need for further exploration in this area.

We used mico-Raman spectroscopy, in conjunction with other techniques such as XRF, XRD, and FT-IR, to conduct a comprehensive analysis of the composition and structural characteristics of fly ash. The objective being to reveal its chemical composition and also assess the potential of spectroscopic techniques in elucidating the morphology and mineralogical composition of fly ash. Corresponding mineral phases were isolated through mineral phase separation techniques, and spectroscopic techniques were employed to explore the distinctive features of the composition of these mineral phases.

2. Experimental

2.1. Materials

The main reagents used in this study are hydrochloric acid (of analytical grade, purchased from Sinopharm Chemical Reagent Co., Ltd.) and sodium hydroxide (also of analytical grade, purchased from Aladdin Biochemical Technology Co., Ltd.). Fly ash samples were collected from two power plants in Guizhou Province, China: the Tangzai Thermal Power Plant (hereinafter referred to as M1) and the Zhijin Thermal Power Plant (denoted as M2). The fly ash was obtained following rigorous pretreatment processes, including efficient dust removal, drying in a vacuum oven at 105 °C for 2 hours, and subsequent processing under vacuum for analysis.

2.2. Mineral phase separation

This study employed a wet magnetic separation technique to segregate the raw fly ash into magnetic (iron-rich microspheres) (Dai *et al*. 2010, Zhang *et al*. 2019, Hou *et al*. 2017) and non-magnetic components. Subsequently, a combined acid-base methodology was utilized for the pre-desilication of the non-magnetic components, aiming to isolate the crystalline phase (mullite-quartz phase) present within them. The combined acid-base experiment involved alternating between three alkali and two acid leaching processes, each with distinct conditions. The initial alkali leaching step was conducted at 95 °C, with a solid-to-liquid ratio of 3 mL/g, using a NaOH concentration of 240 g/L for 60 minutes. The subsequent two alkali leaching processes were performed at 80 °C, with a solid-to-liquid ratio of 5 mL/g and a NaOH concentration of 120 g/L, each lasting 60 minutes. The conditions for acid leaching processes were carried out for 60 minutes at 75 °C with a solid-to-liquid ratio of 4 mL/g and an HCl concentration at 2.73 mol/L.

2.3. Analytical methods

The qualitative and quantitative analysis of the major components in fly ash was conducted using a confocal microscope instrument (Finder 930, Zolix Instruments Co., Ltd., Beijing), X-ray fluorescence spectroscopy (AXIOS, Panalytical, Netherlands). To examine the phase structure of the fly ash, X-ray diffraction (D8 Advance, Bruker Technology Co., Ltd.) and Fourier-transform infrared spectroscopy (ALPHA II, Bruker Technology Co., Ltd.) were employed.

Micro-Raman spectroscopy was utilized to measure the Raman spectra of the fly ash, with an excitation wavelength of 532 nm. The sampling points for sample M1 were designated as 1-i (where i=1, 2, 3, 4), while those for sample M2 were labeled 2-j (where j=1, 2, 3, 4). After the separation of the mullite-quartz phase (denoted as f1 and f2, respectively) from samples M1 and M2, the corresponding sampling points were assigned as f1-i (i=1, 2, 3) and f2-j (j=1, 2, 3), respectively. Similarly, the sampling points for the iron-rich microsphere phase (denoted as g1 and g2, respectively), also isolated from samples M1 and M2, were identified as g1-i (i=1, 2, 3, 4) and g2-j (j=1, 2, 3). A simple flowchart illustrating the analytical process is shown in Figure 1.

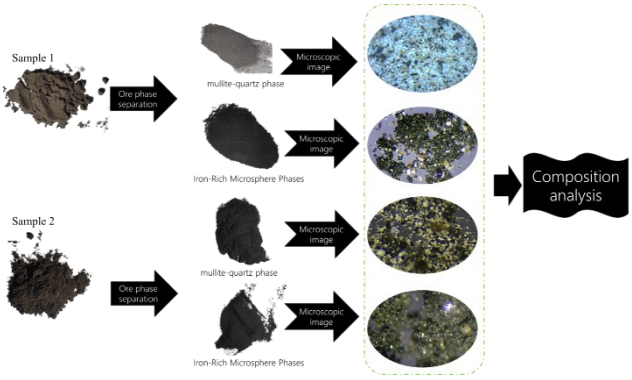

Figure 1. A flowchart showing the application of micro-Raman spectroscopy in the identification of mineral phase composition in fly ash

3. Results and discussion

3.1. Morphology and Composition Analysis of Fly Ash

In this study, the morphology and elemental composition of fly ash were analyzed by confocal microscopic imaging

and SEM-EDS technology, and the elemental and oxide composition of fly ash were further analyzed by XRF. The results are shown in Figure 2 and Table 1.

Figure 2 shows images of two fly ash samples captured at 100x magnification under a confocal microscope (a-b) and SEM-EDS images (c-d). It could be clearly seen from these images that fly ash was mainly composed of spherical particles. At the same time, due to the differences in coal sources and technological conditions, the element content of fly ash in the two power plants is slightly different. But these spherical particles were rich in oxygen (O), silicon (Si), aluminum (Al), iron (Fe), and carbon (C), along with some small amounts of calcium (Ca) and titanium (Ti). In addition, the particles appear in different colors under light, including translucent tones and some black, gold and deep red particles, indicating the presence of different minerals with different chemical compositions and crystal structures in the fly ash. Upon characterizing the fly ash through XRF analysis, the results were tabulated in Table 1. It was discovered that the fly ash was predominantly composed of SiO_2, Al_2O_3, and Fe_2O_3, which collectively accounted for over 80% of its chemical composition. Specifically, SiO_2 existed in the form of quartz and silicate minerals, Al_2O_3 was commonly found in aluminosilicate minerals, and Fe_2O_3 typically occurred in minerals such as hematite.

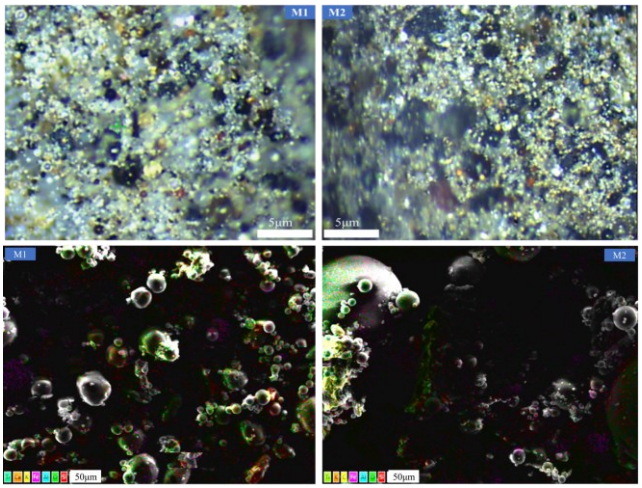

Figure 2. (a)-(b): Microscopic images of fly ash and (c)-(d): SEM-EDS images of fly ash

Table 1. The XRF results of the main chemical ingredients in fly ash

Sample	Ingredients (%)						
	SiO_2	Al_2O_3	Fe_2O_3	CaO	TiO_2	K_2O	SO_3
M1	46.932	29.043	10.71	4.752	2.909	2.558	2.262
M2	48.217	24.312	16.295	2.024	3.961	2.881	1.51

3.2. Basic structure of fly ash

The mineral composition of fly ash is complex, primarily encompassing amorphous phases (chiefly glass phases and residual carbon particles) and crystalline phases (Yan *et al*. 2018). XRD analysis provides valuable information on the crystal structure characteristics of various substances. In this study, XRD technology was utilized to examine the crystal structure of two fly ash samples, and the results are shown in Figure 3a.

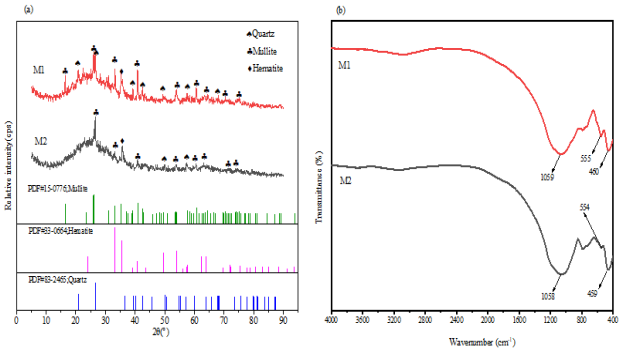

Figure 3. (a) XRD results of fly ash and (b) FT-IR results of fly ash

The primary crystalline phases identified in both fly ash samples were quartz and mullite. Furthermore, a minor quantity of hematite was present in both samples. However, no magnetite peaks were discernible in the spectra, which could potentially be attributed to the low magnetite content in the fly ash thus resulting in a difficulty to test (The content of iron microbeads measured in M1 and M2 fly ash samples were 9.56% and 10.78%, respectively). The study also revealed the presence of a broad peak within the 2θ range of 20°-30°, accompanied by a high background in the diffraction pattern. This characteristic peak is an indicator showing potential existence of glass bodies, unburned carbon particles, and other uncrystallized oxides within the fly ash(Ward and French 2006, Oiu *et al*. 2008) . Correspondingly, similar broad peaks were observed in the XRD spectra of both fly ash samples in this study.

The XRD analysis conducted above enables the determination of the primary crystalline phase components in fly ash. However, regarding the identification of amorphous states, no definitive pattern for peaks associated with amorphous glass featuring regular atomic arrangements has been established in XRD studies(Kirkpatrick *et al*. 1997) . Consequently, this study employs FT-IR spectroscopy to more precisely analyze the amorphous phase components present in fly ash. The results are shown in Figure 3b. The FT-IR spectra of the two fly ash samples exhibit considerable similarity, suggesting a comparable composition between them. Each spectrum from each sample shows three distinctive absorption peaks, indicative of internal vibrations within aluminosilicate structures. Specifically, the absorption peaks observed at 460 cm^{-1} for sample M1 and 459 cm^{-1} for sample M2 are attributed to the bending vibrations of Si-O or Al-O bonds(Fernández-Jiménez and Palomo 2005) . The peaks located at 1058 cm^{-1} and 1059 cm^{-1}, respectively, stem from the asymmetric stretching vibrations of Si-O-Si or Si-O-Al linkages(Mozgawa *et al*.

2014) .Furthermore, the absorption peaks within the 550-850 cm^{-1} range are influenced by the degree of polymerization of the aluminosilicate structure(Bai *et al*. 2008) . Notably, the peaks within this region for both fly ash samples in this study are relatively weak, signifying a significant amount and weak polymerization effect of the amorphous phase in fly ash. Therefore, it can be inferred that fly ash contains a substantial quantity of aluminosilicate glass.

3.3. Mico-Raman spectroscopy analysis of fly ash

3.3.1. Results of raw fly ash

Based on the XRF and XRD analysis data, fly ash is shown to contain a substantial quantity of both crystalline and amorphous aluminosilicates. Figure 4 shows the Raman spectra of two fly ash samples, with Figures 4(a) and 4(b) displaying the microscopic images of these samples, and Figures 4(c) and 4(d) show the Raman spectra of samples M1 and M2, respectively.

In Figure 4(c), distinct peaks are observed at 468 cm^{-1}, 471 cm^{-1}, 471 cm^{-1}, and 468 cm^{-1} for particles 1-1, 1-2, 1-3, and 1-4 of sample M1. These peaks are likely associated with the vibrational modes of bridging oxygen within the Si-O-Si, Si-O-Al, and Al-O-Al bonds in the tetrahedral structure, as reported in(Xie 2008, Silva *et al*. 2012) . Notably, particle 1-4 exhibits no other prominent peaks besides the one at 468 cm^{-1}, which is attributed to the bending vibration of bridge oxygen in the silicon-oxygen tetrahedron structure commonly found in quartz crystals (Guedes *et al*. 2008, Pan *et al*. 2006). Additionally, the Raman spectrum of particle 1-2 displays weak peaks at 781 cm^{-1} and 897 cm^{-1}, with 897 cm^{-1} related to the precise stretching vibration of the Si-O structure. The Raman shift at 781 cm^{-1} may be attributed to the influence of aluminum incorporation into the Si-O structure, causing a shift from the typical 800-1200 cm^{-1} region to lower frequencies, as discussed in(Pan *et al*. 2006, McMillan *et al*. 1982) . Furthermore, peaks observed at 333 cm^{-1} and 211 cm^{-1} in particles 1-1, 1-2, and 1-3 are likely due to the bending vibration of the Al-O structure(Xie 2008) , indicating that particles 1-1, 1-2, and 1-3 represent distinct aluminosilicate structures.

Figure 4(d) shows the Raman spectra of particles in sample M2, it is noteworthy that based on XRD, XRF, and FT-IR analyses, the compound composition of sample M2 is similar to that of sample M1, comprising a high proportion of amorphous aluminosilicate glasses alongside other crystalline and amorphous components. In particular, the peak at 326 cm^{-1} in particle 2-1 is likely caused by the bending vibration of the Al-O structure. Meanwhile, peaks observed at 467 cm^{-1}, 462 cm^{-1}, and 467 cm^{-1} in particles 2-1, 2-3, and 2-4, respectively, are attributed to the bending vibration of bridging oxygen within the Si-O structure. Peaks at 727 cm^{-1} and 766 cm^{-1} in particles 2-1 and 2-4 are indicative of the symmetric stretching vibration of the Al-O structure(Mysen 1996) , while the peak at 909 cm^{-1} in particle 2-3 is possibly caused by the symmetric stretching vibration of the Si-O structure(Xie 2008) [21]. Notably, two distinct broad peaks are also observed at 1344 cm^{-1} and 1582 cm^{-1} in particle 2-2, which have been reported to be associated with unburned amorphous carbon (Guedes *et al*. 2008).

Overall, the presence of Raman peaks confirms the abundance of aluminosilicate or silicate crystals and amorphous crystals in fly ash, further validating the existence of glass phases and mullite-quartz phases. However, the absence of Raman peaks related to Fe-O structures in these spectra can be attributed to the low content of iron-bearing minerals in fly ash.

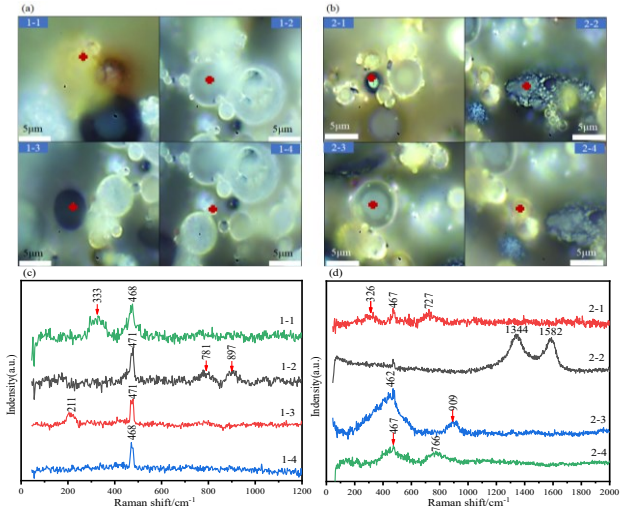

Figure 4. Raman spectra results of fly ash: (a) Tested locations from M1, corresponding to Raman spectra of (c); Tested locations from M2, corresponding to Raman spectra of (d)

3.3.2. Results from the mullite-quartz phase

It has shown that a high proportion of amorphous phases, which can be divided into amorphous aluminosilicate matrix and amorphous silica, along with a small and variable number of crystalline phases (mullite and quartz), constitute the primary components of fly ash(Yan *et al*. 2018) .After the non-magnetic components of M1 and M2 samples in this study were treated with the acid-base pre-treatment method, the amorphous phase was effectively dissolved, and finally crystalline phase substances (mainly mullite and quartz) were obtained. Moreover, the content of crystalline substances accounted for 26.22% and 29.24% respectively, so the content of amorphous substances was higher.

Figure 5 shows the results of the micro-Raman spectroscopy and XRD spectra of the mullite-quartz phase. Figure 5(a-b) show the locations tested in microscopic images of the mullite-quartz phase (Mf1 and Mf2), corresponding to the Raman spectra shown in Figures 5(c-d). Figure 5(e) shows the XRD spectra of the mullite-quartz phase.

As illustrated in Figure 5(c), the prominent peak observed at 469 cm^{-1} in the Raman spectrum of particle f1-2 from sample M1 is attributed to the bending vibration of bridging oxygen within the silicon-oxygen tetrahedron structure, characteristic of quartz crystals(Silva *et al*. 2012) . In contrast, the Raman spectrum of particle f1-1 exhibits weak peaks at 279 cm^{-1} and 935 cm^{-1}, stemming from the bending vibration and symmetric stretching

vibration of the Al-O structure, respectively. Additionally, the peak at 470 cm^{-1} arises from the bending vibration of the Si-O structure. Similarly, in the spectrum of particle f1-3, a sharp peak at 468 cm^{-1} is observed, assigned to the bending vibration of the Si-O structure, while a small sharp peak at 764 cm^{-1} is attributed to the symmetric stretching vibration of the Al-O structure (Pan 2006). The disparities in the Al-O and Si-O structures between particles f1-1 and f1-3 lead to distinct differences in their Raman spectra, suggesting that particles f1-1 and f1-3 are likely mullite crystals with varying crystal structures.

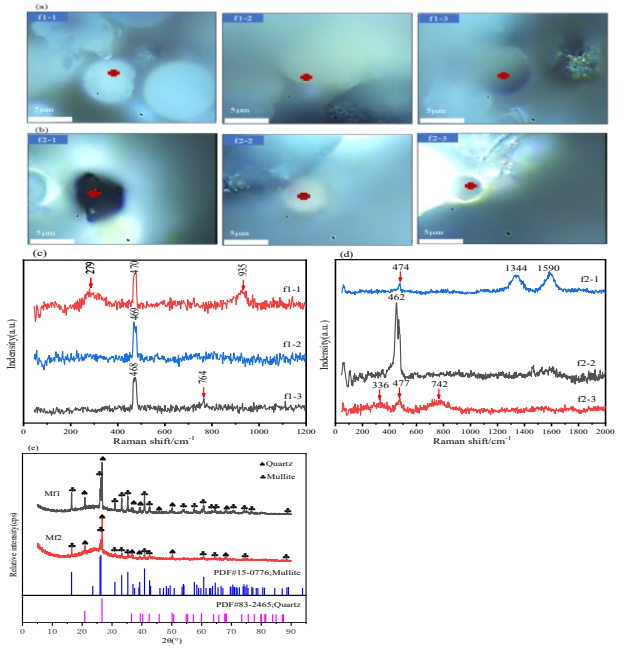

Figure 5. Raman spectra results of fly ash: (a) Tested locations from Mf1, corresponding to Raman spectra of (c); Tested locations from Mf2, corresponding to Raman spectra of (d); (e) XRD results of mullite-quartz phase in Mf1 and Mf2

Figure 5(d) shows the Raman spectra of sample M2, a sharp peak at 462 cm^{-1} is evident in the spectrum of particle f2-2. This peak is attributed to the bending vibration of the Si-O structure and corresponds to the characteristic peak of quartz crystals. Furthermore, the Raman spectrum of particle f2-1 exhibits characteristic peaks of amorphous organic carbon at 1344 cm^{-1} and 1590 cm^{-1}, along with a peak at 474 cm^{-1} resulting from the bending vibration of the Si-O structure, indicating that this particle is a mixture of silicates and amorphous carbon(Guedes *et al*. 2008, Moseenkov *et al*. 2023). Finally, in the spectrum of particle f2-3, a small sharp peak at 477 cm^{-1} signifies the presence of Si-O structures, while weak broad peaks at 336 cm^{-1} and 742 cm^{-1} are indicative of Al-O structures (Xie 2008, Pan 2006), confirming that this particle is a mullite crystal.

Figure 5(e) shows the XRD spectra of mullite-quartz phase of fly ash of two samples. Compared with the XRD pattern of fly ash in Figure 3(a), the characteristic diffraction peak of mullite-quartz phase at 20-30° is significantly weakened, indicating that the glass phase and other amorphous substances in the raw ash are effectively removed after the combined acid-base leaching method. The results show that the main crystal substances in the treated mullite quartz phase are mullite and quartz, which correspond to the results of Raman spectrum analysis above. XRD cannot effectively detect the small impurities in the substance, and for the mineral mixture of fly ash, the composition is more complex, its detection is not effective at this time, but the microscopic imaging in the micro-Raman technology can easily identify the small impurities and trace minerals and generate the corresponding Raman signal. For example, in the Raman spectroscopy, the presence of amorphous carbon was identified, while in the XRD analysis, due to the small content of carbon particles in the fly ash and its high amorphous components it cannot be effectively detected. At the same time, Raman spectroscopy can also provide information about the morphology of elements and symmetry of structures of mullite with different structures. Overall, the micro-Raman spectroscopy analysis of the mullite-quartz phase in two fly ash samples reveals that, upon the removal of the glass phase from the non-magnetic component, the primary crystalline components of fly ash show different structures for mullite and quartz, along with the presence of unburned amorphous carbon.

3.3.3. Results of Iron-Rich Microsphere Phase

Research has shown that the magnetic components primarily consist of iron oxides and amorphous silicates(Kutchko and Kim 2006) . Figure 6 shows the Raman spectra and XRD spectra of the iron-rich microsphere phase from two samples, where Figures 6(a) and 6(b) show the tested locations in microscopic images of Mg1 and Mg2. Figures 6(c) and 6(d) show the Raman spectra corresponding to above locations in the two samples. The XRD spectra are shown in Figure 6(e).

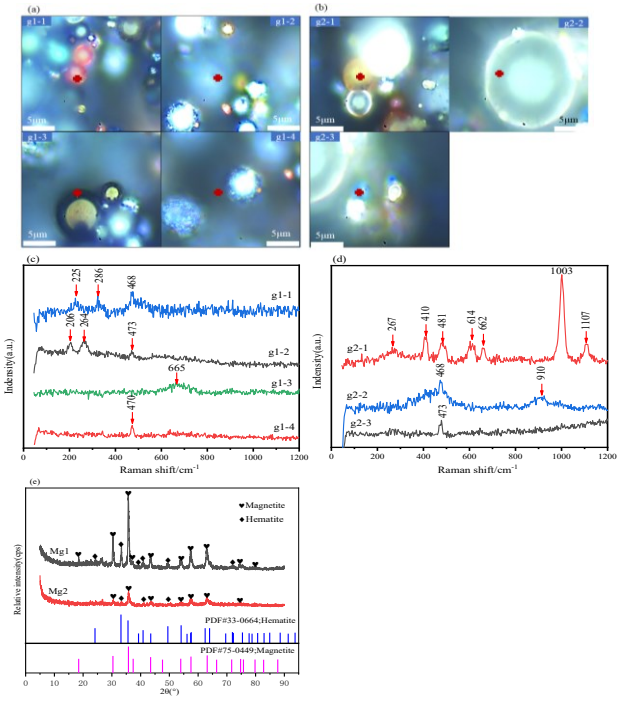

Figure 6. Raman spectra results of fly ash: (a) Tested locations from Mg1, corresponding to Raman spectra of (c); Tested locations from Mg2, corresponding to Raman spectra of (d); (e) XRD results of mullite-quartz phase in Mg1 and Mg2

In Figure 6(c), the Raman spectrum of the iron-rich microsphere phase of sample M1 indicates Raman shifts at 225 cm^{-1} and 286 cm^{-1} in particle g1-1, signifying the bending vibration of the Fe-O structure, which aligns with the characteristic peaks of hematite(Legodi and de Waal 2007, Das and Hendry 2011). Additionally, a sharp peak is observed at 468 cm^{-1}, which is not attributed to hematite's spectrum, possibly indicating the presence of amorphous impurities. It is therefore speculated that this peak arises from Si-O structures. The peak at 473 cm^{-1} in particle g1-2 is attributed to the symmetrical bending vibration of the Si-O structure. The two peaks at approximately 206 cm^{-1} and 264 cm^{-1} are associated with the bending vibration of the Al-O structure, suggesting that these particles may be some form of aluminosilicate crystal or amorphous material (Pan 2006). Particle g1-3 exhibits a broad peak at 665 cm^{-1}, which coincides with the characteristic Raman spectrum of magnetite. However, in natural magnetite, two weak band peaks are typically present at 295 cm^{-1} and 521 cm^{-1}, which are absent in this particle, possibly due to interference from other minerals (Das and Hendry 2011). In particle g1-4, a prominent sharp peak at 470 cm^{-1} is evident, resembling the characteristic peak of quartz associated with the bending vibration of bridge oxygen. However, the peak frequency here is notably higher than that of quartz, potentially influenced by other mineral components affecting the Si-O bridge oxygen vibration. Overall, the iron microsphere phase comprises a silicate crystal or an amorphous structure.

Table 2. Assignments of the Raman bands obtained in the studied particles

Fly ash					
Particles	**Wavenumber (cm^{-1})**	**Assignment**	**Particles**	**Wavenumber (cm^{-1})**	**Assignment**
1-1	468	Si-O (sym bend)	2-1	326, 727	Al-O(bend)、Al-O-Si
	333	Al-O(bend)		467	Si-O (sym bend)
1-2	781	Al-O-Si	2-2	1344, 1582	Amorphous carbon
	471, 897	Si-O (sym bend and sym.str)	2-3	909	Si-O (sym.str)
1-3	471	Si-O (sym bend)		462	Si-O (sym. bend)
	211	Al-O(bend)	2-4	467	Si-O (sym. bend)
1-4	468	Si-O(bend)		766	Al-O-Si
Mullite-Quartz Phase					
Particles	Wavenumber (cm^{-1})	Assignment	Particles	Wavenumber (cm^{-1})	Assignment
f1-1	279, 935	Al-O (bend and sym.str)	f2-1	1344, 1590	Amorphous carbon
	470	Si-O (sym. bend)		474	Si-O
f1-2	469	Si-O(bend)	f2-2	462	Si-O(bend)
f1-3	468	Si-O (sym. bend)	f2-3	336, 742	Al-O (bend and sym.str)
	764	Al-O(sym.str)		477	Si-O (sym. bend)
Iron-Rich Microsphere Phase					
Particles	Wavenumber (cm^{-1})	Assignment	Particles	Wavenumber (cm^{-1})	Assignment
g1-1	225, 286	Fe-O (sym.str and sym. bend)	g2-1	267, 410, 481, 614, 662	–
	468	Si-O(bend)		1003, 1107	–
g1-2	206, 264	Al-O(bend)	g2-2	468	Si-O (sym. bend)
	473	Si-O (sym. bend)		910	Si-O (asym. str)
g1-3	665	Maghemite (sym. str)	g2-3	473	Si-O(bend)
g1-4	470	Si-O (sym. bend)	—	—	—

note:(sym.str), (asym. str), (sym. bend) and (bend) stand for symmetric tensile vibration, asymmetric tensile vibration, symmetric bending vibration and bending vibration mode, respectively

Figure 6(d) shows the Raman spectrum of sample M2. The Raman spectrum of particle g2-1 in sample M2 reveals several distinct sharp peaks within the 200-1200 cm^{-1} range. Meanwhile, through microscopic Raman images of this particle, we could find that the particles showed a spherical shape, the formation of this type of particle is related to the combustion conditions of coal, coal, and power plant combustion technology. However, the specific composition of this particle could not be determined. The Raman spectrum of particle g2-2 displays distinct peaks at 468 cm^{-1} and 910 cm^{-1}, which correspond to the symmetric bending vibration and non-bridging oxygen symmetric stretching vibration of the Si-O structure, respectively, indicating that this particle may be a silicate glass. For particle g2-3, a sharp peak at 473 cm^{-1} is observed in the Raman spectrum, akin to the spectrum of g1-4 from sample M1, suggesting that this particle may also belong to a certain type of silicate crystal or amorphous material.

Figure 6(e) shows the XRD spectra of iron microbeads of two fly ash samples. It was found that the main crystal structure of the iron microbead phase was magnetite and

hematite, and a relatively obvious hump was still found at 20-25°, indicating the existence of glass in the iron microbead phase(Hu *et al*. 2018), which was consistent with the results of the microscopic Raman analysis. Overall, the analysis of Raman spectra shows that the iron microsphere phase is mainly composed of a composite structure of silicate, aluminosilicate glass, magnetite and hematite.

Table 2 lists the Raman shifts and corresponding structures of each particle in this study. Due to the complexity of the composition of fly ash, it was impossible to determine the composition ratio of Al, Si and O in aluminosilicate amorphous glass and aluminosilicate crystal. Although the position of Raman peaks of aluminosilicate crystals and amorphous crystals is similar to some extent, the Raman peaks of aluminosilicate crystals (especially mullite and quartz) can be obtained more accurately after the aluminosilicate glass is effectively removed by acid-base combination method. In addition, we observe that the characteristic Raman peak of quartz crystal appears to be around 464cm^{-1}, and no other significant spectral peak is found in this region. As for the identification of iron oxides and unburned amorphous carbon particles, combined with the detailed observation of particle morphology and XRD characterization results provides a more accurate assessment.

4. Conclusions

This study employed micro-Raman spectroscopy in conjunction with other advanced analytical methods such as XRF, XRD, and FT-IR to analyze the mineral composition of fly ash. The results indicate that the primary chemical constituents of fly ash were primarily composed of SiO_2, Al_2O_3, and Fe_2O_3, with the dominant crystalline minerals being mullite and quartz, which contained aluminosilicate and silicate components, respectively. Micro-Raman spectroscopy analysis of the isolated mineral phases revealed minerals that were challenging to identify in raw fly ash samples. Specifically, it identified hematite, magnetite and glass within the iron-rich microsphere phase, as well as organic carbon components within the mullite-quartz phase. Furthermore, the confirmation of mullite and quartz as the crystalline minerals present in the mullite-quartz phase underscores the accuracy of the analysis. These findings underscore the capability of micro-Raman spectroscopy in efficiently analyzing glass phase structures and other phases, with its high-resolution chemical mapping and the confocal microscopic imaging properties are crucial for reliably characterizing the mineralogical properties of fly ash.

Conflict of interest

The authors declare no conflict of interest, financial or otherwise.

Acknowledgements

This work is financially supported by Guizhou Provincial Science and Technology Plan Project (Grant No. Qiankehe Support [2023] General 157) and Scientific Research Fund of Hunan Provincial Education Department（No. 21A0324）

Reference

Abbas Y., Yun S.N., Wang K.J., Zhang X.M., Jamil M.S., Shah F.A., Zhang X.X., Gao Y.Y. and Luo H. (2024). Association of magnetic-flyash in anaerobic co-digestion for biomethane optimization: Promoting biofilm formation. *Journal of Cleaner Production,* **438**.

Bai J., Li W. and Li B.Q. (2008). Characterization of low-temperature coal ash behaviors at high temperatures under reducing atmosphere. *Fuel,* **87**(4–5), 583–591.

Bandopadhyay A.K. (2010). Determination of quartz content for Indian coals using an FTIR technique. *International Journal of Coal Geology,* **81**(1), 73–78.

Bao Y.P. (2023). Preparation and characterization of fly ash magnetic beads. *Mining Technology,* **23**(01), 235–241.

Dai S.F., Zhao L., Peng S.P., Chou C.L., Wang X.B., Zhang Y., Li D. and Sun Y.Y. (2010). Abundances and distribution of minerals and elements in high-alumina coal fly ash from the Jungar Power Plant, Inner Mongolia, China. *International Journal of Coal Geology,* **81**(4), 320–332.

Das S. and Hendry M.J. (2011), Application of Raman spectroscopy to identify iron minerals commonly found in mine wastes. *Chemical Geology,* **290**(3–4), 101–108.

Egole C.P., Nzebuka G.C., Ufodike C.O., Medupin R.O., Ugwuegbu C.C., Nnodum N.A. and Ochieze U.P.J.J.o.A.E.S. (2024). Experimental characterization of two clay deposits blended with feldspar and quartz for building services and refractory applications. *Journal of African Earth Sciences,* **218**, 105373.

Fernández-Jiménez A. and Palomo A. (2005). Mid-infrared spectroscopic studies of alkali-activated fly ash structure. *Microporous and Mesoporous Materials,* **86**(1–3), 207–214.

Gadore V., Mishra S.R., Sillanpää M. and Ahmaruzzaman M. (2024). Emerging applications of waste fly ash for remediation of environmental contaminants: a high-value and sustainable approach towards utilization of waste materials. *Nanotechnology for Environmental Engineering,* **9**(2), 207–237.

Guedes A., Valentim B., Prieto A.C., Sanz A., Flores D. and Noronha F. (2008). Characterization of fly ash from a power plant and surroundings by micro-Raman spectroscopy. *International Journal of Coal Geology,* **73**(3–4), 359–370.

Hou X., Liang S., Liu Z., Zhang J., Huang R. and Wu Z. (2017). Chemical phase analysis of glass content in fly ash. *Bulletin of the Chinese Ceramic Society,* **36**(11), 3587–3594.

Hu P.P., Hou X.J., Zhang J.B., Li S.P., Wu H., Damo A.J., Li H.Q., Wu Q.S. and Xi X.G. (2018). Distribution and occurrence of lithium in high-alumina-coal fly ash. *International Journal of Coal Geology,* **189**, 27–34.

Kirkpatrick R.J., Yarger J.L., McMillan P.F., Yu P. and Cong X.D. (1997). Raman spectroscopy of C-S-H, tobermorite, and jennite. *Advanced Cement Based Materials,* **5**(3–4), 93–99.

Kumble P., Prashant S. and H M J. (2024). Properties of flyash-dolomite powder-mangalore tile waste powder based alkali-activated binder cured in ambient condition. *Emergent Materials*: 1–17.

Kutchko B.G. and Kim A.G. (2006). Fly ash characterization by SEM-EDS. *Fuel,* **85**(17–18), 2537–2544.

Legodi M.A. and de Waal D. (2007). The preparation of magnetite, goethite, hematite and maghemite of pigment quality from mill scale iron waste. *Dyes and Pigments,* **74**(1): 161–168.

McMillan P., Piriou B. and Navrotsky A. (1982). A raman-spectroscopic study of glasses along the joins silica-calcium aluminate, silica-sodium aluminate, and silica-potassium aluminate. *Geochimica Et Cosmochimica Acta,* **46**(11), 2021–2037.

Moseenkov S.I., Kuznetsov V.L., Zolotarev N.A., Kolesov B.A., Prosvirin I.P., Ishchenko A.V. and Zavorin A.V. (2023). Investigation of Amorphous Carbon in Nanostructured Carbon Materials (A Comparative Study by TEM, XPS, Raman Spectroscopy and XRD). *Materials,* **16**(3), 1112.

Mozgawa W., Krol M., Dyczek J. and Deja J. (2014). Investigation of the coal fly ashes using IR spectroscopy. *Spectrochimica Acta Part a-Molecular and Biomolecular Spectroscopy,* **132**, 889–894.

Mysen B. (1996). Haploandesitic melts at magmatic temperatures: In situ, high-temperature structure and properties of melts along the join $K_2Si_4O_9K_2$ $(KAl)_4O_9$ to 1236°C at atmospheric pressure. *Geochimica Et Cosmochimica Acta,* **60**(19), 3665–3685.

Niyogi A., Pati J., Panigrahi M., Panda D., Chakarvorty M. and Parthasarathy G.J.J.o.A.S. (2018). Raman, infrared, and chemical characterization of fly ash-generated spherules. *Journal of Applied Spectroscopy,* **85**, 856–863.

Oiu M., Yao Z., Zhai Y., Yang G. and Zhang A. (2008). Microanalysis of fly ash by SEM and EDS. *Journal of Chinese Electron Microscopy Society,* (02), 112–116.

Pan F. (2006). A Study of Raman Spectra of Aluminosilicate Minerals.Glass and Melts. China University of Geosciences.

Pan F., Yu X., Mo X., You J., Wang C., Chen H. and Jiang G. (2006) Raman Active Vibrati ons of Aluminosilicates. *Spectroscopy and Spectral Analysis,* (10), 1871–1875.

Polavaram K.C. and Garg N. (2021). Enabling phase quantification of anhydrous cements via Raman imaging. *Cement and Concrete Research,* **150**, 106592.

Saha D., Clarke J.S., Altman S.H., McCann M.A., Kamara R.S., Gordy A., Kervick T.J.S. and Technology P. (2025). Selective extraction and recovery of rare earth elements from coal fly ash by carboxylated mesoporous carbon. *Separation and Purification Technology,* **354**, 129153.

Silva L.F.O., Sampaio C.H., Guedes A., de Vallejuelo S.F.O. and Madariaga J.M. (2012). Multianalytical approaches to the characterisation of minerals associated with coals and the diagnosis of their potential risk by using combined instrumental microspectroscopic techniques and thermodynamic speciation. *Fuel,* **94**(1), 52–63.

Tiwari M., Sahu S., Bhangare R., Ajmal P., Pandit G.J.A.R. and Isotopes. (2014). Elemental characterization of coal, fly ash, and bottom ash using an energy dispersive X-ray fluorescence technique. *Applied Radiation and Isotopes,* **90**, 53–57.

Vassilev S.V., Vassileva C.G.J.E. and Fuels. (2005). Methods for characterization of composition of fly ashes from coal-fired power stations: a critical overview. *Energy & Fuels,* **19**(3), 1084–1098.

Ward C.R. and French D. (2006). Determination of glass content and estimation of glass composition in fly ash using quantitative X-ray diffractometry. *Fuel,* **85**(16), 2268–2277.

Witte A., Garg N.J.C. and Research C. (2024). Particle shape, crystallinity, and degree of polymerization of fly ash via combined SEM-EDS and Raman spectroscopy. *Cement and Concrete Research,* **184**, 107612.

Xie J. (2008). Raman spectroscopy study of hyperfine structure of aluminosilicate and feldspar. Beijing: China University of Geosciences.

Yan K.Z., Guo Y.X., Ma Z.B., Zhao Z.S. and Cheng F.Q. (2018). Quantitative analysis of crystalline and amorphous phases in pulverized coal fly ash based on the Rietveld method. *Journal of Non-Crystalline Solids,* **483**, 37–42.

Zhang J., Li Z., Yang C., Li S. and Li H. (2019). Investigation on the occurrence morphology and quantitative analysis of amorphous silicon in coal fly ash. *Clean Coal Technol,* **25**(03), 116–121.